

25. H. Correia, S. Balseiro, M. De Areia, *J. Comp. Hum. Biol.* **56**, 153 (2005).
26. D. Walrath, thesis, University of Pennsylvania, Philadelphia (1997).
27. C. B. Ruff, *Yearb. Phys. Anthropol.* **37**, 65 (1994).
28. The Gona Project thanks the Authority for Research and Conservation of Cultural Heritage of the Ministry of Culture and Tourism, and the National Museum of Ethiopia, for research permits and support. Support for this research was provided by the L. S. B. Leakey Foundation, National Geographic Society, Wenner-Gren Foundation, and NSF.

We are grateful for the overall support of K. Shick and N. Toth (co-directors of CRAFT). We appreciate the hospitality of the Afar administration at Semera and our Afar colleagues from Eloha. We thank Y. Haile-Selassie and L. Jellema (Cleveland Museum of Natural History) for allowing us to examine materials in their care. Discussions with and comments by C. O. Lovejoy, R. G. Tague, Y. Haile-Selassie, G. Suwa, T. White, G. WoldeGabriel, B. Latimer, B. Asfaw, S. Standen, R. Byrne, and anonymous reviewers were helpful. A. Admasu's help at the National Museum of Ethiopia is appreciated.

Supporting Online Material

www.sciencemag.org/cgi/content/full/322/5904/1089/DC1
Materials and Methods
SOM Text
Figs. S1 to S11
Tables S1 to S10
References

22 July 2008; accepted 14 October 2008
10.1126/science.1163592

Slide into Action: Dynamic Shuttling of HIV Reverse Transcriptase on Nucleic Acid Substrates

Shixin Liu,¹ Elio A. Abbondanzieri,¹ Jason W. Rausch,⁴ Stuart F. J. Le Grice,⁴ Xiaowei Zhuang^{1,2,3*}

The reverse transcriptase (RT) of human immunodeficiency virus (HIV) catalyzes a series of reactions to convert single-stranded viral RNA into double-stranded DNA for host cell integration. This process requires a variety of enzymatic activities, including DNA polymerization, RNA cleavage, strand transfer, and strand displacement synthesis. We used single-molecule fluorescence resonance energy transfer to probe the interactions between RT and nucleic acid substrates in real time. RT was observed to slide on nucleic acid duplexes, rapidly shuttling between opposite termini of the duplex. Upon reaching the DNA 3' terminus, RT can spontaneously flip into a polymerization orientation. Sliding kinetics were regulated by cognate nucleotides and anti-HIV drugs, which stabilized and destabilized the polymerization mode, respectively. These long-range translocation activities facilitate multiple stages of the reverse transcription pathway, including normal DNA polymerization and strand displacement synthesis.

Retroviral reverse transcriptase (RT) is a multifunctional enzyme that catalyzes conversion of the single-stranded viral RNA genome into integration-competent double-stranded DNA. RT possesses several distinct activities, including DNA- and RNA-dependent DNA synthesis, DNA-directed RNA cleavage, strand transfer, and strand displacement synthesis, all of which are required to complete the reverse transcription cycle (fig. S1) (1, 2). The enzyme first uses viral RNA as the template to synthesize minus-strand DNA (3, 4), and the resulting DNA/RNA hybrid is then cleaved by the ribonuclease H (RNase H) activity of RT to produce short RNA fragments hybridized to nascent DNA (5, 6). Specific RNA fragments, known as the polypurine tracts (PPTs), serve as primers for synthesis of plus-strand DNA from the minus-strand DNA template (7–9). Secondary structures present in the viral RNA genome, as well as the nontemplate strands hybridized to the DNA template, require RT to perform strand displacement synthesis during both minus- and plus-strand DNA synthesis (10–16).

As a major target for anti-HIV therapy, RT has been the subject of extensive research. Crystal structures, biochemical assays, and single-molecule analyses have suggested different modes of interaction between RT and nucleic acid substrates, providing snapshots of the nucleoprotein complexes that illuminate the functional mechanism of RT [e.g., (17–25)]. Nevertheless, how the enzyme-substrate complex acquires specific functional configurations and switches between different functional modes remains unclear. For example, how does RT efficiently locate the 3' terminus of nascent DNA on a long duplex substrate to initiate DNA polymerization? This question is particularly important for a low-processivity polymerase such as RT, which must frequently locate the polymerization site after dissociation (10, 26). Perhaps even more puzzling is how the dissociated RT locates the polymerization site during strand displacement synthesis, considering that the primer terminus may itself be displaced from the template by the competing nontemplate strand. Also, RT cleaves at many different sites within a DNA/RNA hybrid, but how it accesses these sites remains incompletely understood (21, 22). A dynamic visualization of RT interacting with different substrates will help us address these questions and gain a more complete understanding of its function.

In this work, we used fluorescence resonance energy transfer (FRET) (27, 28) to monitor in real time the action of individual HIV-1 RT molecules

and their interactions with various nucleic acid substrates. We specifically labeled RT with the FRET donor dye Cy3 at either the RNase H domain (H-labeled) or the fingers domain (F-labeled) of its catalytically active p66 subunit (fig. S2A) (2, 29, 30). A Glu⁴⁷⁸→Gln⁴⁷⁸ (E478Q) mutation was introduced to eliminate RNase H activity (31) and prevent degradation of the nucleic acid substrates during experiments. Nucleic acid substrates were labeled with the FRET acceptor dye Cy5 at various sites, specifically immobilized on a quartz surface, and immersed in a solution containing Cy3-labeled RT (fig. S2B) (2). Fluorescence from individual RT-substrate complexes was monitored with a total-internal-reflection fluorescence (TIRF) microscope by using an alternating laser excitation scheme (32). The observed FRET value allowed the binding configuration of the enzyme to be determined (fig. S2C) (2). Control experiments showed that neither dye labeling nor surface immobilization notably affected the enzyme activity (fig. S3) and that photophysical properties of the FRET dyes did not change appreciably when placed in proximity to the enzyme (fig. S4) (2).

To mimic substrates encountered by RT during minus-strand synthesis, we constructed a series of hybrid structures of various lengths, each consisting of a DNA primer and an RNA template with Cy5 attached to one of two sites: (i) near the 3' end of the RNA template, which we define as the back end of the hybrid (“back-labeled,” Fig. 1, A to C), or (ii) near the 5' end of the RNA template and 3' end of the DNA primer, which we define as the front end (“front-labeled,” fig. S5, B and C) (2). On a 19–base pair (bp) hybrid, a length chosen to approximate its footprint on nucleic acid duplexes (17, 33), RT bound in only one configuration: Binding of H-labeled RT to the back-labeled substrate yielded uniformly high FRET values (centered at 0.95) (Fig. 1A), indicating that RT bound with its RNase H domain close to the back end of the hybrid. Considering that the RNase H and polymerase active sites are at opposite ends of the substrate binding cleft of RT, this configuration places the polymerase active site of the RT over the 3' terminus of the DNA primer, consistent with the polymerization-competent binding mode observed in crystal structures (17, 18).

In contrast, two distinct binding modes were observed on longer DNA/RNA hybrids. H-labeled RT bound to back-labeled 38-bp hybrid yielded two FRET peaks centered at 0.95 and 0.39, re-

¹Department of Chemistry and Chemical Biology, Harvard University, Cambridge, MA 02138, USA. ²Department of Physics, Harvard University, Cambridge, MA 02138, USA. ³Howard Hughes Medical Institute, Harvard University, Cambridge, MA 02138, USA. ⁴HIV Drug Resistance Program, National Cancer Institute, Frederick, MD 21702, USA.

*To whom correspondence should be addressed. E-mail: zhuang@chemistry.harvard.edu

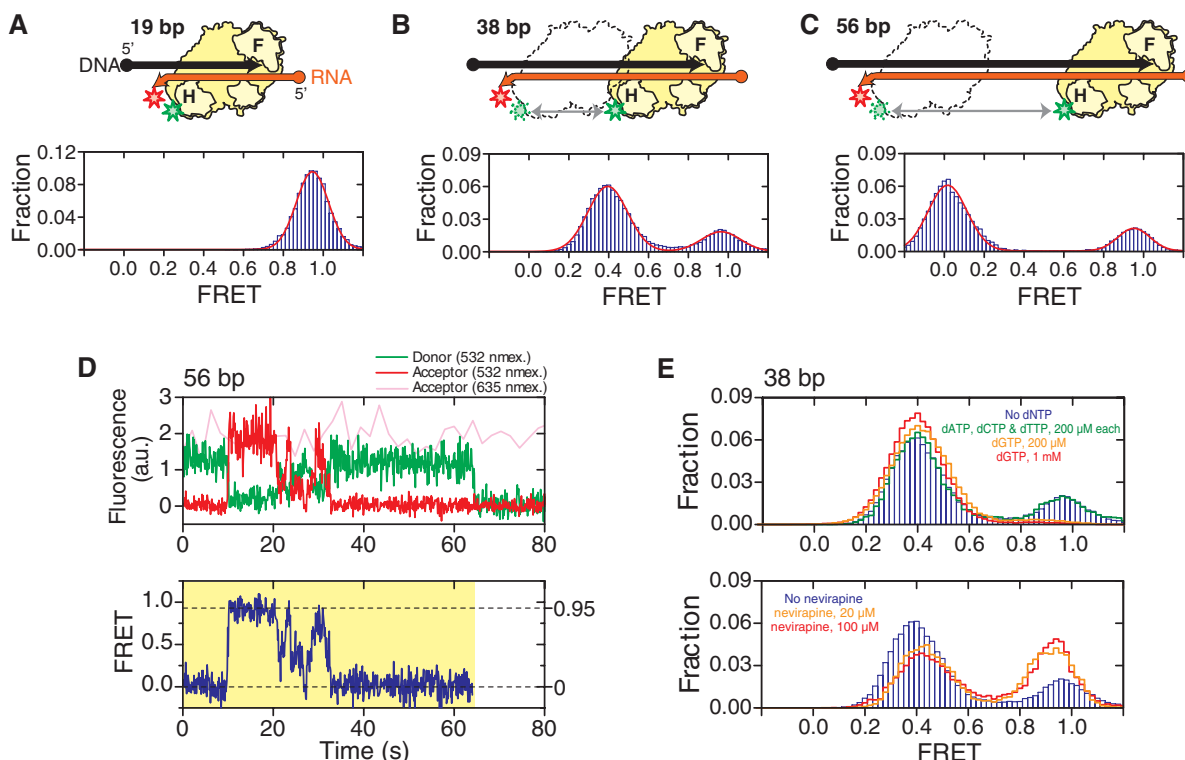
spectively (Fig. 1B). The FRET value of 0.39 is quantitatively consistent with RT binding in polymerization competent mode, in which the polymerase active site is located over the primer terminus at the front end of the hybrid, placing the Cy3 dye ~19 bp away from the Cy5 label. The high-FRET peak at 0.95 indicates an additional binding mode in which the RNase H domain is located near the back end of the hybrid, which apparently cannot support polymerase activity. The equilibrium constant between the front- and back-end binding states was 3.3:1. Moving the biotin from the 5' end of the DNA primer (i.e.,

near the back end of the hybrid) to the 5' end of the RNA template (i.e., near the front end) resulted in a nearly identical equilibrium constant (3.1:1), again suggesting a minimal effect of surface immobilization. These two binding modes at the front and back end of the hybrid were further confirmed by two additional FRET labeling schemes in which F-labeled or H-labeled RT was added to the front-labeled substrate (fig. S5) (2). The two end-binding states also predict further separation of the two FRET peaks as the length of the hybridized region increases, which was experimentally confirmed with a 56-bp

hybrid. Binding of H-labeled RT to the back-labeled 56-bp hybrid produced two FRET peaks centered at 0 and 0.95, also with a ~3:1 partition ratio (Fig. 1C).

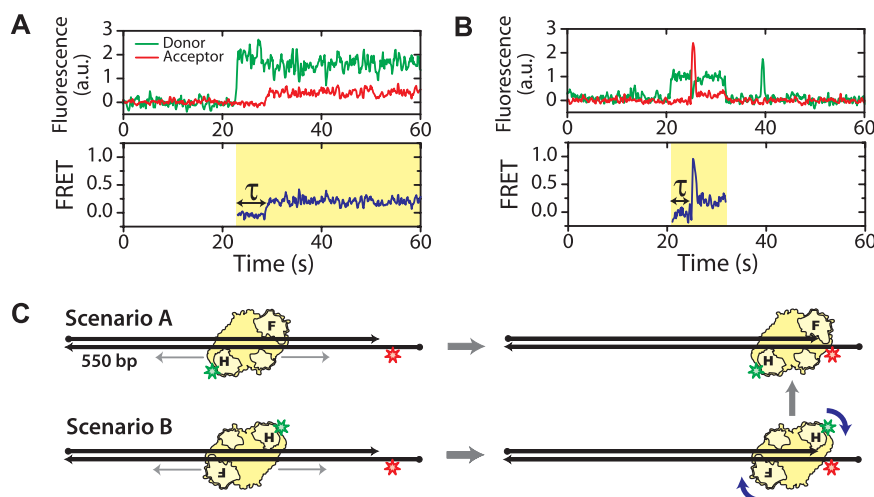
Taken together, these results indicate that the enzyme can stably bind either to the front end of the hybrid poised for DNA extension or to the back end, placing the RNase H domain close to the 3' end of the RNA template. The front-end binding state of RT should also support RNase H activity. The two binding modes were independent of hybrid sequence and the nature of the hybrid termini, that is, whether they feature recessed

Fig. 1. RT slides on nucleic acid substrates. (A to C) H-labeled RT (yellow) bound to a 19-bp (A), 38-bp (B), and 56-bp (C) back-labeled DNA (black)/RNA (orange) hybrid. F and H on the enzyme represent the fingers and RNase H domains, respectively. Circle and arrow on the nucleic acid strands represent 5' and 3' ends, respectively. Green and red stars indicate Cy3 and Cy5 dyes, respectively. The FRET histograms (blue) were fit with a single (A) or double [(B) and (C)] Gaussian peaks (red line). (D) Representative fluorescence (top) and FRET (bottom) time traces of RT bound to a 56-bp DNA/RNA hybrid at 12°C, showing gradual transitions between the 0 and 0.95 FRET states and the preferred intermediates near FRET ~ 0.3 to 0.5. The time resolution is 10 Hz. The green and red traces represent donor and acceptor fluorescence under 532-nm excitation, and the pink trace represents acceptor fluorescence under 635-nm excitation. The yellow shade marks a single RT binding event. a.u., arbitrary units. (E) Effects of nucleotides and nevirapine



on sliding. (Top) FRET histograms of RT bound to the 38-bp DNA/RNA hybrid in the absence of nucleotides (blue), in the presence of the cognate dGTP (orange and red), or noncognate nucleotides (green). The DNA primer was chain-terminated to prevent elongation. (Bottom) FRET histograms in the absence (blue) and presence of nevirapine (orange and red).

Fig. 2. Sliding of RT facilitates polymerization site targeting. H-labeled RT was added to a ~550-bp DNA duplex with Cy5 attached near the front end. Binding of RT to the polymerization site at the duplex front end is expected to give a FRET value of 0.3. (A) Donor and acceptor fluorescence and corresponding FRET time traces of a typical binding event show a time delay (τ) between binding of RT and placing of RT at the polymerization site. (B) A binding event showing a transient 0.9 FRET state between the 0 and 0.3 FRET states, suggesting that RT arrived at the front end in an orientation that placed the RNase H domain close to the primer terminus and subsequently flipped to the polymerization orientation. The time resolution of the traces is 10 Hz. Cy5 fluorescence under direct 635-nm excitation (omitted for clarity) indicates that an active Cy5 is present during the whole detection time. Yellow shades in the FRET time traces mark individual RT binding events. The histogram of the time delay, τ , is shown in fig. S9. (C) Schematic depiction of the two primer terminus search scenarios as suggested by traces in (A) and (B).



DNA or RNA (fig. S6) (2). They were also independent of whether the RNase H-inactivating E478Q mutation was introduced (fig. S5) (2). To further test whether sliding was a general activity of RT, we exchanged the RNA template in the DNA/RNA hybrid for a DNA template to emulate plus-strand DNA synthesis. RT was again observed to slide between the termini of the duplex DNA, although the transition rates between the two ends were different from those observed on the DNA/RNA hybrid (fig. S7) (2).

The FRET time traces of individual RT molecules showed repeated transitions between the front- and back-end bound states within a single binding event (Fig. 1D), suggesting shuttling between the two ends of the hybrid without dissociation. The FRET transitions between the two end states were not instantaneous but rather gradual, with preferred intermediate states in the middle of the hybrid (Fig. 1D and fig. S8, A and B) (2). Shuttling motion sped up as the temperature was raised (fig. S8C) but did not require nucleotide hydrolysis, suggesting that the movement is a thermally driven diffusion process. RT was previously observed to cleave RNA at multiple po-

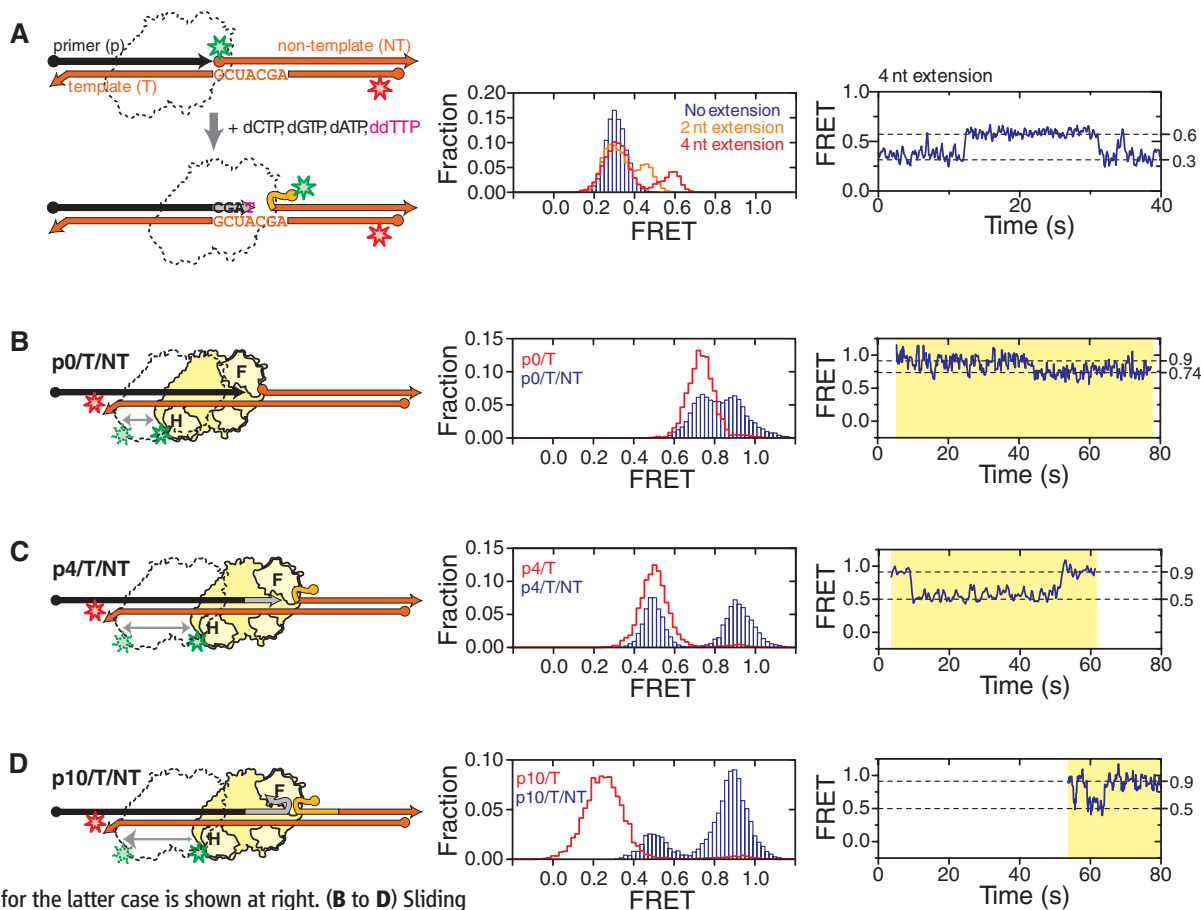
sitions within a DNA/RNA hybrid (5, 21, 22) in a manner consistent with the end-binding states and the sliding intermediates observed here, suggesting that sliding may provide a mechanism for RT to rapidly access these cleavage sites.

It is remarkable that a polymerase could frequently slide away from the polymerization site. To explore what structural rearrangements within the enzyme may be required for this action, we tested the effects of small molecule ligands on sliding kinetics. Binding of a cognate nucleotide is expected to cause the fingers and thumb domains of RT to form a tighter grip around the primer terminus (34) and stabilize the polymerization state. To test the effect of nucleotide binding, we again used H-labeled RT and back-labeled 38-bp DNA/RNA hybrid but with 3'-dideoxynucleoside-terminated DNA primer to prevent DNA synthesis. Addition of 2'-deoxyguanosine 5'-triphosphate (dGTP), the next cognate nucleotide, significantly stabilized the low FRET front-end bound state (Fig. 1E), further supporting the notion that the front-end bound state reflects RT binding in the polymerization-competent mode. Kinetically, addition of 1 mM dGTP slowed down

the rate constant of front to back transitions ($k_{\text{front} \rightarrow \text{back}}$) by 12-fold without substantially affecting the reverse rate constant $k_{\text{back} \rightarrow \text{front}}$ (fig. S7C) (2). In contrast, addition of mismatched nucleotides [2'-deoxyadenosine 5'-triphosphate (dATP), 2'-deoxycytidine 5'-triphosphate (dCTP), and 2'-deoxythymidine 5'-triphosphate (dTTP)] did not significantly affect the transition kinetics (Fig. 1E). Another small molecule ligand tested was the nonnucleoside RT inhibitor (NNRTI), one of the major classes of anti-HIV drugs that inhibit DNA synthesis (30, 35). We measured the sliding dynamics of RT in the presence of nevirapine, a representative NNRTI. Interestingly, the effects of the drug were opposite to those of the cognate deoxyribonucleotide triphosphate (dNTP): Addition of nevirapine destabilized the front-end bound state of the enzyme (Fig. 1E) by increasing $k_{\text{front} \rightarrow \text{back}}$ without significantly altering $k_{\text{back} \rightarrow \text{front}}$ (fig. S8C) (2). Structurally, NNRTI and cognate dNTP have opposite effects on the conformation of RT near the polymerase active site (34, 35): Whereas nucleotide binding tightens the clamp of the fingers and thumb domains around the substrate, binding of NNRTI loosens

Fig. 3. RNA strand displacement synthesis.

(A) Substrate structural dynamics during strand displacement synthesis. RT and nucleotides were added to Cy3/Cy5 doubly labeled p0/T/NT substrate to initiate synthesis. Overlapping sequence within the p and NT strands are colored in light gray and light orange, respectively. The corresponding FRET histograms are shown in the middle. Blue bars represent the FRET distribution in the presence of RT but absence of nucleotides. The orange line indicates the distribution in the presence of dCTP, ddGTP, dATP, and dTTP; and the red line indicates the distribution in the presence of dCTP, dGTP, dATP, and ddTTP, allowing a two- and a four-nucleotide extension, respectively. A representative FRET time trace for the latter case is shown at right. **(B to D)** Sliding of RT during RNA strand displacement synthesis. **(B)** H-labeled RT bound to back-labeled p0/T/NT. The corresponding FRET histogram (middle, blue) and representative time trace (right) show dynamic transitions between two FRET states (0.74 and 0.9). Overlaid on the FRET histogram is the FRET distribution of RT bound to the p0/T substrate lacking the NT strand (red line). **(C and D)** As above except that p0/T/NT is replaced by p4/T/NT **(C)** or p10/T/NT **(D)** to mimic the extended substrates encountered during RNA displacement synthesis. The corresponding FRET histograms (middle, blue bars) and time traces (right) show



dynamic transitions between FRET states of 0.5 and 0.9. Overlaid in red lines are the FRET distributions of RT bound to the corresponding pX/T duplex without the NT strand. Yellow shades in the right graphs mark individual RT binding events, all of which started with FRET = 0.9, indicating initial binding to the back end of the pX/T region. Time resolutions of the traces are 10 Hz in **(A)**, **(B)**, and **(D)** and 5 Hz in **(C)**. All measurements were done in the presence of dNTPs, and the primer 3' terminus was chain-terminated to prevent elongation.

the clamp. Hence, our data suggest that relaxation of the fingers-thumb grip is likely required for RT to escape the polymerization site. Our observation that NNRTI promotes enzyme escape from the polymerization site also suggests an inhibitory mechanism for this class of drugs and explains why the inhibitory effect of NNRTI is stronger on long DNA synthesis than on short DNA synthesis (36).

Next, we probed potential functional roles of RT sliding on reverse transcription. Compared to cellular DNA polymerases, RT exhibits poor processivity, typically dissociating from the substrate after synthesizing only a few to a few hundred nucleotides (10, 26), despite a ~10-kb-long HIV genome (37). RT thus frequently encounters the challenge of having to locate the nascent DNA terminus to continue DNA synthesis. The ability of RT to slide on duplexes suggests an interesting mechanism of enzyme targeting by one-

dimensional search, a mechanism that has been proposed for target searching by transcription factors, RNA polymerase, and DNA repair enzyme (38–42). To test this possibility, we added H-labeled RT to a ~550-bp front-labeled DNA duplex (Fig. 2). Were RT to bind directly to the duplex front end, we would expect a FRET value of 0.3 immediately upon binding, corresponding to the ~19-bp distance expected between Cy3 and Cy5. Instead, we found that the majority of the binding events initiated with a FRET value of 0, reaching 0.3 only after a finite time delay (Fig. 2A and fig. S9). This observation indicates that the enzyme first bound to the DNA outside the polymerization site and subsequently moved to the primer terminus where polymerization takes place (Fig. 2C). Such a binding procedure will likely increase the polymerization target searching efficiency on long duplexes where the primer terminus constitutes only a tiny fraction of the duplex sub-

strate. However, if the enzyme can indeed bind in the middle of a duplex, the lack of directional cues may also lead to binding in the “wrong” orientation, such that the RNase H domain is poised closer than the polymerase domain to the 3' terminus of the primer (Fig. 2C). In this case, even after sliding to the front end, RT would not be properly positioned for DNA synthesis. This type of binding was indeed observed frequently (~48% of the time), as indicated by a high FRET state with FRET ~0.9, after the initial 0 FRET state (Fig. 2B). Remarkably, the high FRET state converted rapidly into the 0.3 FRET state in situ without dissociation (Fig. 2B), indicating that the enzyme flipped into the polymerization-competent orientation. The ability of RT to flip to the polymerization orientation once reaching the primer terminus without dissociation may further increase its target searching efficiency. Our data does not exclude a possibility that the enzyme may also flip in the middle of the duplex, although such flipping events should not lead to a net increase of target searching efficiency.

Hairpins and long duplexes present on the template strand during DNA synthesis require the polymerization machinery to perform strand displacement synthesis. Polymerization site targeting on these substrates may be even more challenging because, after enzyme dissociation, these template secondary structures could displace the nascent primer terminus to occlude the polymerization site. This is especially problematic in the case of intrastrand RNA displacement during minus-strand synthesis because duplex RNA is more stable than a DNA/RNA hybrid (43, 44). To probe the structural dynamics of substrates encountered during RNA strand displacement synthesis, we designed a series of FRET-labeled triple-stranded substrates, each consisting of an RNA template (T) to which a complementary DNA primer (p) and RNA nontemplate strand (NT) were simultaneously hybridized, with the Cy3 and Cy5 dyes flanking the T/NT duplex region (Fig. 3A). We use the notation $pX/T/NT$ to represent a substrate whose primer has been extended by X nucleotides. As expected, the FRET distributions for substrates with all X values displayed a peak at 0.3, identical to that observed for the nonextended $p0/T/NT$ substrate (fig. S10), indicating that the T/NT duplex was fully annealed and that the extended DNA primers were not able to displace the NT RNA.

We then added RT and dNTPs to the $p0/T/NT$ substrate to monitor substrate dynamics during displacement synthesis. In the absence of dNTP, a single FRET peak centered at 0.3 was again observed (Fig. 3A). After addition of dNTPs to initiate primer extension and selected dideoxynucleotide triphosphate (ddNTP) to terminate synthesis at specific positions, FRET was observed to increase because of unwinding of the T/NT duplex. The presence of dCTP, ddGTP, dATP, and dTTP supported a two-nucleotide addition, producing a higher FRET peak at 0.45 (Fig. 3A). This higher FRET peak further increased

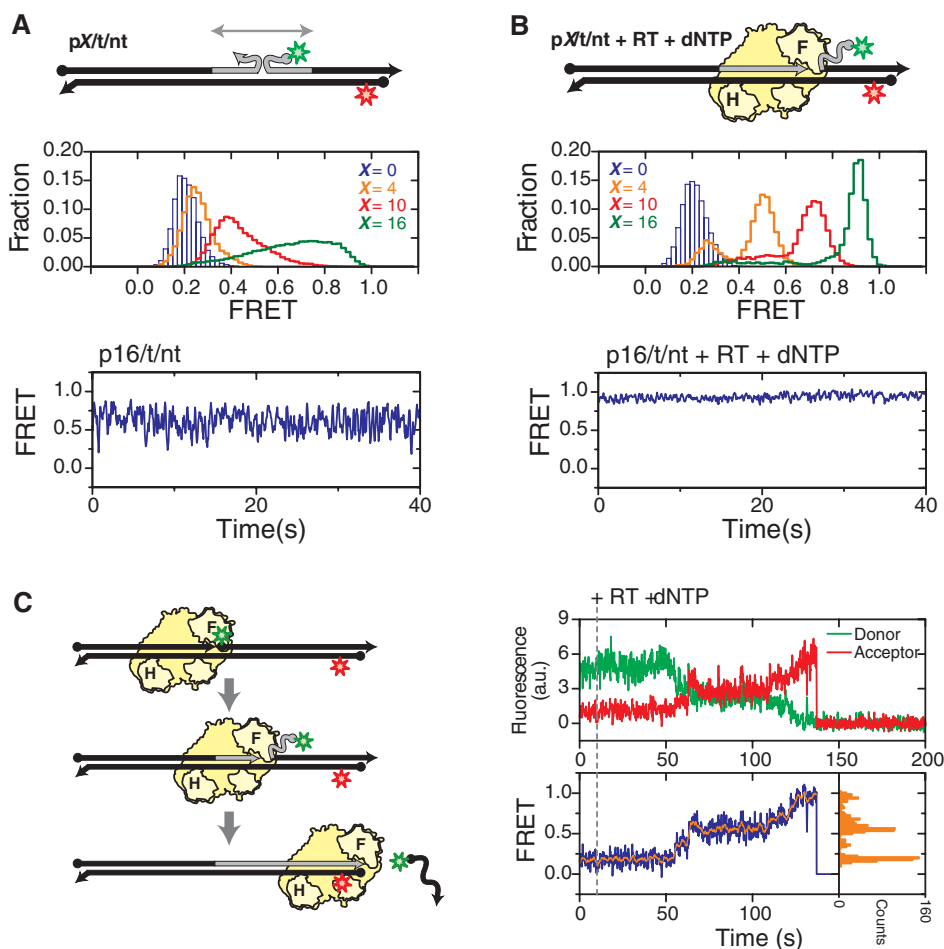


Fig. 4. DNA strand displacement synthesis. (A) Structural dynamics of the $pX/t/nt$ substrates ($X = 0, 4, 10,$ and 16) consisting of all DNA strands. The corresponding FRET histograms are shown in the middle and a representative FRET time trace ($X = 16$) in the bottom. (B) As in (A) but in the presence of RT and dNTPs. The primers were terminated with a dideoxynucleoside to prevent elongation. (C) Single-molecule detection of DNA displacement synthesis. RT and dNTPs were added to the $p0/t/nt$ substrate to initiate DNA synthesis in situ. FRET gradually increased as reaction progressed because of the unzipping of the nontemplate strand. Completion of the reaction was marked by the abrupt loss of the fluorescence signal because of dissociation of the donor labeled nontemplate strand. Plateaus were observed in the donor/acceptor fluorescence traces (top) and the FRET trace (blue trace in bottom left graph), indicating pausing events during synthesis. As a corollary, distinct peaks were observed in the histogram (bottom right inset) constructed from the FRET trace smoothed by 9-point average (orange trace in bottom left graph). Time resolutions are 16 Hz in (A) and (B) and 10 Hz in (C).

to 0.6 in the presence of dCTP, dGTP, dATP, and ddTTP, which allowed a four-nucleotide extension (Fig. 3A). The FRET distribution agreed quantitatively with that observed for the pre-assembled, chain-terminated p4/T/NT substrate in the presence of RT and dNTPs (fig. S11) (2), confirming successful primer extension. FRET time traces of individual molecules showed repetitive transitions between the 0.6 and 0.3 FRET states (Fig. 3A), suggesting frequent reannealing of the T and NT strands.

One possible cause for T/NT reannealing is sliding of RT to the back end of the p/T hybrid, leaving its front end unbound. To test this experimentally, we added Cy3-labeled RT and dNTPs to Cy5-labeled pX/T/NT substrates, the primers of which were chain-terminated to prevent extension (Fig. 3, B to D). Indeed, transitions between a high and a relatively low FRET state were observed. The high FRET state (0.9) indicates proximity of RT to the back end of the p/T hybrid. The lower FRET states (0.74 for p0/T/NT and 0.5 for p4/T/NT) quantitatively agree with those observed for the p0/T and p4/T hybrids lacking the NT strand (Fig. 3, B and C), to which RT should predominantly bind at the front end in the presence of dNTPs. These results indicate that RT shuttles between the polymerization site and the back end of the substrate even during displacement synthesis.

In the absence of enzyme, a stable T/NT RNA duplex was formed (fig. S10) and no spontaneous annealing of the pX/T hybrid was observed in the FRET time traces. The low processivity of RT poses another question: How would the enzyme, after dissociation, locate the polymerization site (i.e., the front end of the primer/template hybrid) again if such a structure is rarely formed? The answer can be found in the FRET traces: The vast majority (~90%) of the binding events on the pX/T/NT substrates started at the back end with high FRET, with RT subsequently sliding forward to assume the front-end binding state with relatively low FRET (Fig. 3C, right). These observations suggest that sliding allows the enzyme to kinetically access the disrupted polymerization site and assist primer-template annealing, thereby facilitating RNA strand displacement synthesis.

Interestingly, on a substrate with a longer primer extension (p10/T/NT), FRET was also observed to switch between the same 0.9 and 0.5 states as observed for the p4/T/NT substrate (Fig. 3D). Had the primer/template hybrid fully annealed, binding of RT to the front end of the hybridized region would yield FRET values significantly lower than 0.5, as observed for the p10/T substrates lacking the NT strand (Fig. 3D). Similar results were found for the p5/T/NT substrate. These data indicate that RT was not able to slide all the way to the front end of the primer once the overlap between the p and NT strands exceeded four nucleotides. Moreover, the enzyme predominantly remained at the back end of the substrate. We thus expect the efficiency of strand displacement synthesis to drop accordingly. This was directly confirmed by an ensemble

primer extension assay, which revealed that primer extension primarily terminated after adding five nucleotides through RNA strand displacement synthesis (fig. S12A) (2). The exact termination sites were sequence-dependent, consistent with previous observations (16).

The energetic difference between the pX/T and T/NT duplexes observed during RNA strand displacement synthesis does not exist in DNA strand displacement synthesis because all strands involved in the latter case are DNA. To examine substrate dynamics during DNA strand displacement synthesis, we doubly labeled all DNA primer/template/nontemplate substrates (defined as pX/t/nt) with Cy3 and Cy5 (Fig. 4A). In contrast to the pX/T/NT counterparts, the FRET distributions were substantially broader for nonzero primer extension ($X = 4, 10, \text{ and } 16$), and rapid FRET fluctuations were observed in single-molecule traces (Fig. 4A). These observations suggest frequent exchanges between the primer and nontemplate strands for base-pairing with the template. After addition of RT and dNTPs to the substrates (chain-terminated to prevent primer extension), the FRET distribution predominantly assumed a high FRET value that consistently increased with X (Fig. 4B), suggesting that RT reached the front end of the p/t duplex and unwound the t/nt duplex. Even in the case of DNA displacement synthesis, the primer was rarely fully annealed to the template in the absence of a bound RT. It is likely that RT is also targeted to the polymerization site by first binding to the intact part of the primer/template duplex and subsequently sliding forward to unwind the nontemplate strand and anneal the primer. Because there is no substantial energy penalty for exchanging DNA base pairs, RT was thus able to access the primer terminus regardless of the length of the primer extension (Fig. 4B), consistent with RT's ability to perform displacement synthesis through long DNA duplexes (12). When RT and dNTPs were added to the non-terminated p0/t/nt substrate to support synthesis, an increase in FRET was observed as the nt strand was displaced (Fig. 4C). Once the FRET donor-labeled nt strand was fully displaced, a sudden drop in the total fluorescence signal reflected completion of the reaction (Fig. 4C). Rapid and complete DNA strand displacement synthesis was observed for nearly all molecules (fig. S12) (2). Frequent pausing was also observed during synthesis, indicated by plateaus in the single-molecule FRET trace (Fig. 4C). The origin of these kinetic pausing events and their relation to the preferred synthesis termination sites (23, 45) will be a subject of future investigation.

HIV-1 RT thus appears to be a highly dynamic enzyme that can spontaneously slide over long distances on DNA/RNA and DNA/DNA duplex structures, which facilitates multiple phases of reverse transcription, including targeting RT to the primer terminus for DNA polymerization, allowing the enzyme to rapidly access multiple sites within an RNA/DNA hybrid during viral RNA degradation, as well as displacing the nontem-

plate strand and annealing the primer terminus during displacement synthesis. The dynamic flexibility further extends into orientational conformations, allowing the enzyme to flip between opposite binding orientations that support different activities (21, 25). Flipping and sliding can be combined in a complex series of enzyme movements to enhance its efficacy: RT molecules originally bound in the opposite orientation were observed to spontaneously flip into the polymerization orientation after sliding to the primer terminus. It is remarkable that an enzyme could have such large-scale orientational and translational dynamics. This type of dynamic flexibility may be a general design principle for multifunctional enzymes like HIV RT, helping them to rapidly access different binding configurations required to accomplish different functions.

References and Notes

1. A. Telesnitsky, S. P. Goff, in *Retroviruses*, J. M. Coffin, S. H. Hughes, H. E. Varmus, Eds. (Cold Spring Harbor Laboratory Press, Cold Spring Harbor, NY, 1997), pp. 121–160.
2. Materials and methods are available as supporting material on Science Online.
3. D. Baltimore, *Nature* **226**, 1209 (1970).
4. H. M. Temin, S. Mizutani, *Nature* **226**, 1211 (1970).
5. J. P. Leis, I. Berkower, J. Hurwitz, *Proc. Natl. Acad. Sci. U.S.A.* **70**, 466 (1973).
6. J. Hansen, T. Schulze, W. Mellert, K. Moelling, *EMBO J.* **7**, 239 (1988).
7. J. K. Smith, A. Cywinski, J. M. Taylor, *J. Virol.* **49**, 200 (1984).
8. C. A. Omer, R. Resnick, A. J. Faras, *J. Virol.* **50**, 465 (1984).
9. W. I. Finston, J. J. Champoux, *J. Virol.* **51**, 26 (1984).
10. H. E. Huber, J. M. McCoy, J. S. Seehra, C. C. Richardson, *J. Biol. Chem.* **264**, 4669 (1989).
11. M. Hottiger, V. N. Podust, R. L. Thimmig, C. McHenry, U. Hubscher, *J. Biol. Chem.* **269**, 986 (1994).
12. S. H. Whiting, J. J. Champoux, *J. Virol.* **68**, 4747 (1994).
13. G. M. Fuentes, P. J. Fay, R. A. Bambara, *Nucleic Acids Res.* **24**, 1719 (1996).
14. Z. Suo, K. A. Johnson, *Biochemistry* **36**, 12459 (1997).
15. C. D. Kelleher, J. J. Champoux, *J. Biol. Chem.* **273**, 9976 (1998).
16. C. Lanciault, J. J. Champoux, *J. Biol. Chem.* **279**, 32252 (2004).
17. A. Jacobo-Molina *et al.*, *Proc. Natl. Acad. Sci. U.S.A.* **90**, 6320 (1993).
18. S. G. Sarafianos *et al.*, *EMBO J.* **20**, 1449 (2001).
19. S. G. Sarafianos *et al.*, *EMBO J.* **21**, 6614 (2002).
20. W. Metzger, T. Hermann, O. Schatz, S. F. Le Grice, H. Heumann, *Proc. Natl. Acad. Sci. U.S.A.* **90**, 5909 (1993).
21. J. J. DeStefano, L. M. Mallaber, P. J. Fay, R. A. Bambara, *Nucleic Acids Res.* **21**, 4330 (1993).
22. M. Wisniewski, M. Balakrishnan, C. Palaniappan, P. J. Fay, R. A. Bambara, *J. Biol. Chem.* **275**, 37664 (2000).
23. J. Winsell, B. A. Paulson, B. D. Buelow, J. J. Champoux, *J. Biol. Chem.* **279**, 52924 (2004).
24. P. J. Rothwell *et al.*, *Proc. Natl. Acad. Sci. U.S.A.* **100**, 1655 (2003).
25. E. A. Abbondanzieri *et al.*, *Nature* **453**, 184 (2008).
26. K. J. Williams, L. A. Loeb, M. Fry, *J. Biol. Chem.* **265**, 18682 (1990).
27. L. Stryer, R. P. Haugland, *Proc. Natl. Acad. Sci. U.S.A.* **58**, 719 (1967).
28. T. Ha *et al.*, *Proc. Natl. Acad. Sci. U.S.A.* **93**, 6264 (1996).
29. Z. Hostomsky, Z. Hostomska, T. B. Fu, J. Taylor, *J. Virol.* **66**, 3179 (1992).
30. L. A. Kohlstaedt, J. Wang, J. M. Friedman, P. A. Rice, T. A. Steitz, *Science* **256**, 1783 (1992).
31. J. W. Rausch, B. K. Sathyanarayana, M. K. Bona, S. F. Le Grice, *J. Biol. Chem.* **275**, 16015 (2000).

32. A. N. Kapanidis *et al.*, *Science* **314**, 1144 (2006).
 33. M. Gotte, G. Maier, H. J. Gross, H. Heumann, *J. Biol. Chem.* **273**, 10139 (1998).
 34. H. Huang, R. Chopra, G. L. Verdine, S. C. Harrison, *Science* **282**, 1669 (1998).
 35. J. Ren *et al.*, *Nat. Struct. Biol.* **2**, 293 (1995).
 36. Y. Quan, C. Liang, P. Inouye, M. A. Wainberg, *Nucleic Acids Res.* **26**, 5692 (1998).
 37. L. Ratner *et al.*, *Nature* **313**, 277 (1985).
 38. P. H. von Hippel, O. G. Berg, *J. Biol. Chem.* **264**, 675 (1989).
 39. H. Kabata *et al.*, *Science* **262**, 1561 (1993).
 40. M. Guthold *et al.*, *Biophys. J.* **77**, 2284 (1999).

S.F.J.L.G.). X.Z. is a Howard Hughes Medical Institute investigator. E.A.A. is a Jane Coffin Childs postdoctoral fellow. Nevirapine was provided through the AIDS Research and Reference Reagent Program of NIH.

Supporting Online Material

www.sciencemag.org/cgi/content/full/322/5904/1092/DC1
 Materials and Methods
 Figs. S1 to S12
 References

11 July 2008; accepted 24 September 2008
 10.1126/science.1163108

Batf3 Deficiency Reveals a Critical Role for CD8 α^+ Dendritic Cells in Cytotoxic T Cell Immunity

Kai Hildner,^{1,2} Brian T. Edelson,¹ Whitney E. Purtha,³ Mark Diamond,¹ Hirokazu Matsushita,¹ Masako Kohyama,^{1,2} Boris Calderon,¹ Barbara U. Schraml,¹ Emil R. Unanue,¹ Michael S. Diamond,^{1,3} Robert D. Schreiber,¹ Theresa L. Murphy,¹ Kenneth M. Murphy^{1,2*}

Although in vitro observations suggest that cross-presentation of antigens is mediated primarily by CD8 α^+ dendritic cells, in vivo analysis has been hampered by the lack of systems that selectively eliminate this cell lineage. We show that deletion of the transcription factor *Batf3* ablated development of CD8 α^+ dendritic cells, allowing us to examine their role in immunity in vivo. Dendritic cells from *Batf3*^{-/-} mice were defective in cross-presentation, and *Batf3*^{-/-} mice lacked virus-specific CD8⁺ T cell responses to West Nile virus. Importantly, rejection of highly immunogenic syngeneic tumors was impaired in *Batf3*^{-/-} mice. These results suggest an important role for CD8 α^+ dendritic cells and cross-presentation in responses to viruses and in tumor rejection.

During antigen cross-presentation (1), antigens generated in one cell are presented by major histocompatibility complex (MHC) class I molecules of a second cell. It remains unclear whether all antigen presenting cells (APCs) use cross-presentation and whether this pathway plays a role in immune responses in vivo (2). Dendritic cells (DCs) are a heterogeneous group of APCs with two major subsets, plasmacytoid dendritic cells (pDCs) and conventional CD11c⁺ dendritic cells (cDCs) (3). Subsets of cDCs include CD8 α^+ , CD4⁺, and CD8 α^- CD4⁻ populations that may exert distinct functions in immune responses. Evidence has suggested that CD8 α^+ cDCs are important for cross-presentation during infections but has its basis in ex vivo analysis (4–6) or in vitro antigen loading (7). Evidence both for and against a role for cross-presentation in responses against tumors has been reported (8–10).

Attempts have been made to study the in vivo role of DCs by selective depletion. Diphtheria toxin treatment can deplete all CD11c^{hi} cells in

one transgenic mouse model (11) but affects splenic macrophages and activated CD8⁺ T cells (12). Gene targeting of transcription factors (e.g., *Irf2*, *Irf4*, *Irf8*, *Stat3*, and *Id2*) has caused broad defects in several DC subsets, T cells, and macrophages (13). To identify genes regulating DC development, we performed global gene expression analysis across many tissues and immune cells (fig. S1A). *Batf3* (also known as *Jun dimerization protein p21SNFT*) (14) was highly expressed in cDCs, with low to absent expression in other immune cells and nonimmune tissues. Thus, we generated *Batf3*^{-/-} mice that lack expression of the *Batf3* protein (fig. S1, B to D).

In spleens of *Batf3*^{-/-} mice, we found a selective loss of CD8 α^+ cDCs, without abnormalities in other hematopoietic cell types or architecture (Fig. 1 and figs. S2 to S14). CD8 α^+ cDCs coexpress DEC205, CD24, and low levels of CD11b (3, 15). *Batf3*^{-/-} mice lacked splenic CD11c^{hi}CD8 α^+ DEC205⁺ cells (Fig. 1A), showed a loss of CD11c^{hi}CD11b^{dull} cells and CD11c^{hi}CD8 α^+ CD24⁺ cells (Fig. 1B), but had normal populations of CD4⁺ and CD8 α^- CD4⁻ cDC subsets (Fig. 1B). Lymph nodes and thymi of *Batf3*^{-/-} mice lacked CD8 α^+ DCs but had normal distributions of CD8 α^- CD11c⁺ cells (Fig. 1C). DEC205^{int} and DEC205^{hi} DCs were present in lymph nodes draining the skin of *Batf3*^{-/-} mice (Fig. 1C) and showed normal migration from skin to lymph node after topical application of fluorescein-5-isothiocyanate (fig. S3A). *Batf3*^{-/-} mice had normal development of pDCs (CD11c^{int}CD11b⁻B220⁺)

(fig. S3B), interstitial DCs of pancreatic islets (CD11c⁺CD8 α^-) (fig. S3, C and D), monocytes, neutrophils (fig. S3E), and SIGN-R1⁺ marginal zone and MOMA-1⁺ metallophilic macrophages (Fig. 2A). CD8 α^+ cDCs developed normally in heterozygous *Batf3*^{+/-} mice (fig. S4A) and were absent in *Rag2*^{-/-} *Batf3*^{-/-} mice (fig. S4B).

This loss of CD8 α^+ cDCs could result from a cell-autonomous hematopoietic defect or a cell-extrinsic requirement for *Batf3*. To distinguish these possibilities, we generated chimeras in which CD45.2⁺ *Batf3*^{+/-} or CD45.2⁺ *Batf3*^{-/-} bone marrow (BM) was transplanted into lethally irradiated CD45.1⁺CD45.2⁺ recipients (Fig. 2B). Upon reconstitution (fig. S5A), we found CD8 α^+ cDCs developed only from *Batf3*^{+/-} donor BM cell (Fig. 2B), indicating a cell-intrinsic hematopoietic defect in *Batf3*^{-/-} mice.

Treatment of mice with fms-like tyrosine kinase 3 (flt3) ligand-Fc (FL-Fc) increased the numbers of CD8 α^+ cDCs, CD8 α^- cDCs, and pDCs in *Batf3*^{+/-} mice but failed to increase the number of CD8 α^+ cDCs in *Batf3*^{-/-} mice (Fig. 2C). In vitro culture of BM with FL generates cell populations corresponding to pDCs (CD11c⁺CD45RA⁺) and cDCs (CD11c⁺CD45RA⁻) (3, 16) (Fig. 2D). These in vitro-derived cDCs do not express CD8 α or CD4 but contain a CD24⁺Sirp- $\alpha^{\text{lo-int}}$ population corresponding to CD8 α^+ cDC (16). *Batf3*^{+/-} or *Batf3*^{-/-} BM cells treated with FL produced similar ratios of pDCs and cDCs (Fig. 2D and fig. S5B). However, *Batf3*^{-/-} BM generated far fewer CD24⁺Sirp- α^+ cells compared with *Batf3*^{+/-} BM (Fig. 2D), corresponding to loss of CD8 α^+ cDCs. Lastly, DCs generated from *Batf3*^{-/-} BM were selectively deficient in Toll-like receptor (TLR) 3-induced interleukin (IL)-12 production (fig. S5C), a specific feature of CD8 α^+ cDCs (16). Similarly, CD11c⁺ cDCs from the spleens of *Batf3*^{-/-} mice were selectively deficient in TLR3-induced IL-12 production but had normal responses to TLR4 and TLR9 ligands (fig. S6A).

We next tested whether APCs from *Batf3*^{-/-} mice could prime CD4⁺ and CD8⁺ T cell responses. Similar proliferative responses of OT-II transgenic CD4⁺ T cells (17) occurred with soluble ovalbumin presented by *Batf3*^{+/-} and *Batf3*^{-/-} cDCs (fig. S6B). However, *Batf3*^{-/-} cDCs were defective in an assay for cross-presentation of cellular antigen to CD8⁺ T cells (2, 18) (Fig. 3A). OT-I T cells proliferated in response to *Batf3*^{+/-} cDCs cocultured with ovalbumin-loaded cells but failed to proliferate in response to *Batf3*^{-/-} cDCs in this assay.

¹Department of Pathology and Immunology, Washington University School of Medicine, 660 South Euclid Avenue, St. Louis, MO 63110, USA. ²Howard Hughes Medical Institute, Washington University School of Medicine, 660 South Euclid Avenue, St. Louis, MO 63110, USA. ³Departments of Medicine and Molecular Microbiology, 660 South Euclid Avenue, St. Louis, MO 63110, USA.

*To whom correspondence should be addressed. E-mail: kmurphy@wustl.edu



Supporting Online Material for

Slide into Action: Dynamic Shuttling of HIV Reverse Transcriptase on Nucleic Acid Substrates

Shixin Liu, Elio A. Abbondanzieri, Jason W. Rausch, Stuart F. J. Le Grice, Xiaowei Zhuang*

*To whom correspondence should be addressed. E-mail: zhuang@chemistry.harvard.edu

Published 14 November 2008, *Science* **322**, 1092 (2008)

DOI: 10.1126/science.1163108

This PDF file includes:

Materials and Methods
Figs. S1 to S12
References

Materials and Methods

RT preparation. Dye-labeled RT was derived from either the wildtype enzyme or an RNase H inactive mutant in which an E478Q mutation was introduced into the RNase H domain (1). To produce the H-labeled RT, the native cysteines on RT were changed to serine and a unique cysteine residue was introduced at the C-terminus of the p66 subunit to allow specific labeling of dye molecules. To create the F-labeled RT, one of the native cysteines at position 38 of the p66 subunit was retained for dye labeling. The p51 subunit of RT, which primarily serves a structural scaffolding role, was not labeled. Purified RT molecules were incubated with Cy3 maleimide (GE Healthcare) for 60 minutes in 100 mM pH 7.0 NaH₂PO₄/Na₂HPO₄ buffer. Cy3-labeled RT was then dialyzed for more than 48 hours to remove excess dye molecules.

Nucleic acid preparation. Synthetic DNA (Operon or IDT) and RNA (Dharmacon) oligonucleotides were purified by denaturing polyacrylamide gel electrophoresis. When necessary, the strands were specifically derivatized with a biotin or an amino modifier during synthesis. Cy3 or Cy5 mono-reactive NHS ester (GE Healthcare) was post-synthetically conjugated to the primary amine group on DNA or RNA. Labeled oligonucleotides were HPLC purified by reverse phase chromatography on a C8 column (GE Healthcare).

To assemble a primer/template duplex of less than 60 bp in length, the two strands were annealed at a mixing ratio of 1:1, heated to 95 °C for 5 minutes, and slowly cooled to room temperature over 1 hour in annealing buffer (50 mM pH 8.0 Tris-HCl, 100 mM KCl, and 1 mM EDTA). To generate the ~550 bp duplex DNA, a short duplex (31 bp) modified with biotin and Cy5 was first annealed as above and then ligated by T4 DNA ligase (New England Biolabs) to a long duplex (~520 bp) generated by PCR. Both pieces contained an EcoRI restriction site and were digested by EcoRI (New England Biolabs) before ligation. The ligation product was gel purified.

To assemble a primer/template/non-template construct, the 3 strands were annealed with a 1:2:3 ratio in the annealing buffer using a Bio-Rad thermocycler with the following program: 1 minute at 95 °C, 10 minutes ramp to 70 °C, 30 minutes at 70 °C, 10 minutes ramp to 33 °C, 30 minutes at 33 °C, and finally cooling to and holding at 4 °C (2). The 1:2:3 mixing ratio was chosen to minimize the number of free primer molecules and primer/template complexes without the non-template strand. Annealed products were analyzed on 5% native polyacrylamide gels at

4 °C to confirm successful assembly. Removal of unannealed or partially assembled constructs was not necessary as they lacked biotin groups for surface immobilization or dye molecules for detection.

Single-molecule FRET measurement. Nucleic acid substrates were immobilized on PEG-coated quartz microscope slides through biotin-streptavidin linkage as previously described (3). The biotin group was placed at the 5' end of the DNA primer in all constructs unless otherwise mentioned. The surface-immobilized Cy5-labeled substrates were immersed in a solution containing Cy3-labeled RT (Fig. S2B). The fluorescence signals for the FRET donor Cy3 and acceptor Cy5 were detected using a prism-type TIRF microscope. Alternating 532 nm and 635 nm laser light were used to excite the sample. In 9 out of every 10 frames, the FRET donor Cy3 was excited by a 532 nm Nd:YAG laser (Crystal Laser), and every tenth frame, allowing us to probe FRET between the Cy3-labeled RT and Cy5-labeled substrates, a 635 nm laser (Coherent) was used to excite Cy5 directly to confirm the presence of active-Cy5 labeled substrate independent of RT binding. Emission from the donor and acceptor were separated using a dichroic mirror (Chroma Technology) and imaged onto the two halves of a back-illuminated electron multiplying CCD camera (Andor Ixon 887). Each RT binding event caused an increase in the total Cy3 and Cy5 fluorescence signals under the 532 nm excitation (Fig. S2C). The FRET value during the binding events was defined as $I_A/(I_A + I_D)$, where I_A and I_D were the fluorescence signals detected from the acceptor and donor channel, respectively. Single-step RT dissociation or Cy3 photobleaching indicated the binding of a single enzyme. Measurements were performed at room temperature (23 °C) unless otherwise specified. The imaging buffer contained 50 mM pH 8.0 Tris-HCl, 50 mM KCl, 6 mM MgCl₂, and 0.1 mg/ml BSA (New England Biolabs) except for experiments shown in Figure 2, where the imaging buffer contained 25 mM pH 8.0 Tris-HCl, 25 mM KCl, 3 mM MgCl₂, 30% v/v glycerol, and 0.1 mg/ml BSA. An oxygen scavenger system (10% w/v glucose, 300 µg/ml glucose oxidase, and 40 µg/ml catalase) and a reducing reagent (2 mM Trolox) was also included in the imaging buffer to minimize photobleaching and blinking (4).

During data acquisition, Cy3-labeled RT was added to surface-immobilized Cy5-labeled nucleic acid substrates. The concentration of Cy3-labeled p66 subunits used in the single-molecule experiments was 10 – 20 nM. A large excess of unlabeled wildtype p51 subunits were added such that the majority of Cy3-labeled p66 form heterodimers with p51. This strategy was

used to ensure that the concentration of the dye-labeled p66 in the solution did not overwhelm single molecule detection of RT-substrate complexes bound to the surface. As the p66 and p51 subunits alone exhibited much lower affinities to the nucleic acid substrates, the majority of the binding events observed involved a p66/p51 heterodimer. The observation of single-step RT dissociation or Cy3 photobleaching ensured the binding of a single enzyme. To monitor structural dynamics of the nucleic acid substrates, unlabeled RT was added to the Cy3 and Cy5 doubly labeled substrates.

Kinetic analysis of RT sliding. During the process of sliding, RT dwelt substantially longer at either end of the duplex than in the middle positions. We thus describe sliding kinetics by a simple model featuring four first-order rate constants as described in Fig. S7C: $k_{\text{front} \rightarrow \text{off}}$, dissociation rate constant from the front end of the duplex; $k_{\text{front} \rightarrow \text{back}}$, the transition rate constant from the front end to the back end; $k_{\text{back} \rightarrow \text{front}}$, the transition rate constant from the back end to the front end; $k_{\text{back} \rightarrow \text{off}}$, dissociation rate constant from the back end of the duplex. Assuming that the system was at equilibrium, the rate constants were calculated using the following formulae:

$$k_{\text{front} \rightarrow \text{off}} = (1/\tau_{\text{front}})P_{\text{front} \rightarrow \text{off}}, \quad k_{\text{front} \rightarrow \text{back}} = (1/\tau_{\text{front}})P_{\text{front} \rightarrow \text{back}},$$

$$k_{\text{back} \rightarrow \text{front}} = (1/\tau_{\text{back}})P_{\text{back} \rightarrow \text{front}}, \quad k_{\text{back} \rightarrow \text{off}} = (1/\tau_{\text{back}})P_{\text{back} \rightarrow \text{off}},$$

where τ_{front} and τ_{back} are the mean dwell times of RT at the front end and back end, respectively, which were derived from the FRET time traces. $P_{\text{front} \rightarrow \text{off}}$ is the probability of dissociation once RT is bound to the front end, $P_{\text{front} \rightarrow \text{back}}$ is the probability of sliding to the back end once RT is bound to the front end, $P_{\text{back} \rightarrow \text{front}}$ is the probability of sliding to the front end once RT is bound to the back end, $P_{\text{back} \rightarrow \text{off}}$ is the probability of dissociation once RT is bound to the back end. These probabilities were derived from FRET time traces using the following equations:

$$P_{\text{front} \rightarrow \text{off}} = \frac{\text{the number of front-end binding events that are followed by a dissociated event}}{\text{the total number of front-end binding events}},$$

$$P_{\text{front} \rightarrow \text{back}} = \frac{\text{the number of front-end binding events that are followed by a back-end binding event}}{\text{the total number of front-end binding events}},$$

$$P_{\text{back} \rightarrow \text{front}} = \frac{\text{the number of back-end binding events that are followed by a front-end binding event}}{\text{the total number of back-end binding events}},$$

$$P_{\text{back} \rightarrow \text{off}} = \frac{\text{the number of back-end binding events that are followed by a dissociated event}}{\text{the total number of back end binding events}}.$$

Bulk primer extension assay. The primer/template and primer/template/non-template substrates were annealed as described above. Cy5 (GE Healthcare) was conjugated to the primers to monitor DNA synthesis. Substrates (5 nM) were incubated with RT (20 nM) in RT reaction buffer (50 mM pH 8.0 Tris-HCl, 50 mM KCl, and 6 mM MgCl₂) at room temperature for 5 minutes in a final reaction volume of 100 μ l. DNA synthesis was initiated by addition of the four dNTPs (each at 200 μ M final concentration) and terminated by mixing 5 μ l aliquot of the reaction mixture with 15 μ l of stop buffer (96% formamide, 20 mM EDTA) at the time points indicated in the text. Reaction products were heated to 95 °C for 5 minutes, fractionated over a 10% denaturing polyacrylamide gel, and quantified using a Typhoon Trio Imager (GE Healthcare).

Supporting Figures

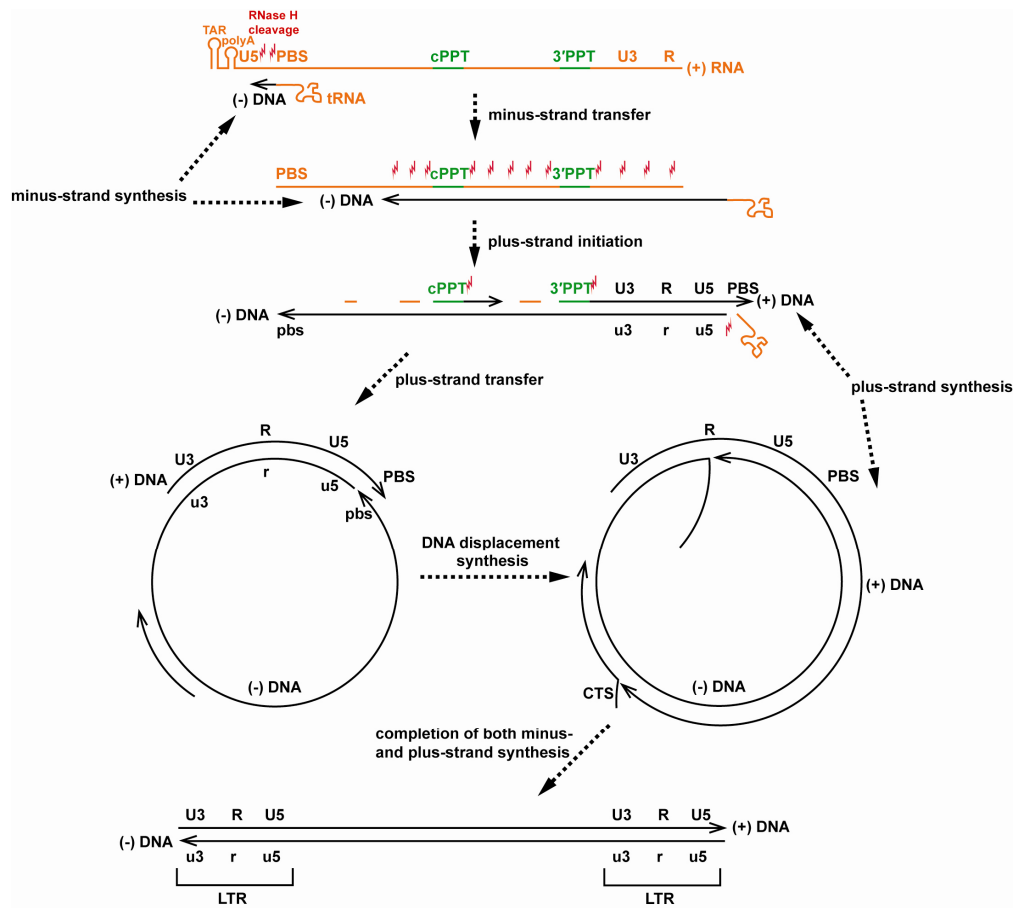


Fig. S1. Schematic of the HIV-1 reverse transcription pathway (5). RT initiates minus-strand DNA synthesis from a cellular tRNA hybridized to the primer binding site (PBS) located near the 5' terminus of viral RNA. During and following minus-strand synthesis, viral RNA is hydrolyzed via the RNase H activity of RT, leaving two specific RNA fragments, known as the polypurine tracts (PPTs), to serve as unique primers for initiation of plus-strand DNA synthesis. As plus-strand DNA synthesis proceeds, the linear replication intermediate circularizes via PBS homology, and RT performs DNA displacement synthesis to complete the genome conversion process. The final product of reverse transcription is a double-stranded proviral DNA flanked by long terminal repeat (LTR) sequences, which are subsequently recognized by the viral integrase protein for insertion into chromosomal DNA of the infected cell. TAR: trans-activation response element; cPPT: central polypurine tract; 3'PPT: 3' polypurine tract; CTS: central termination sequence.

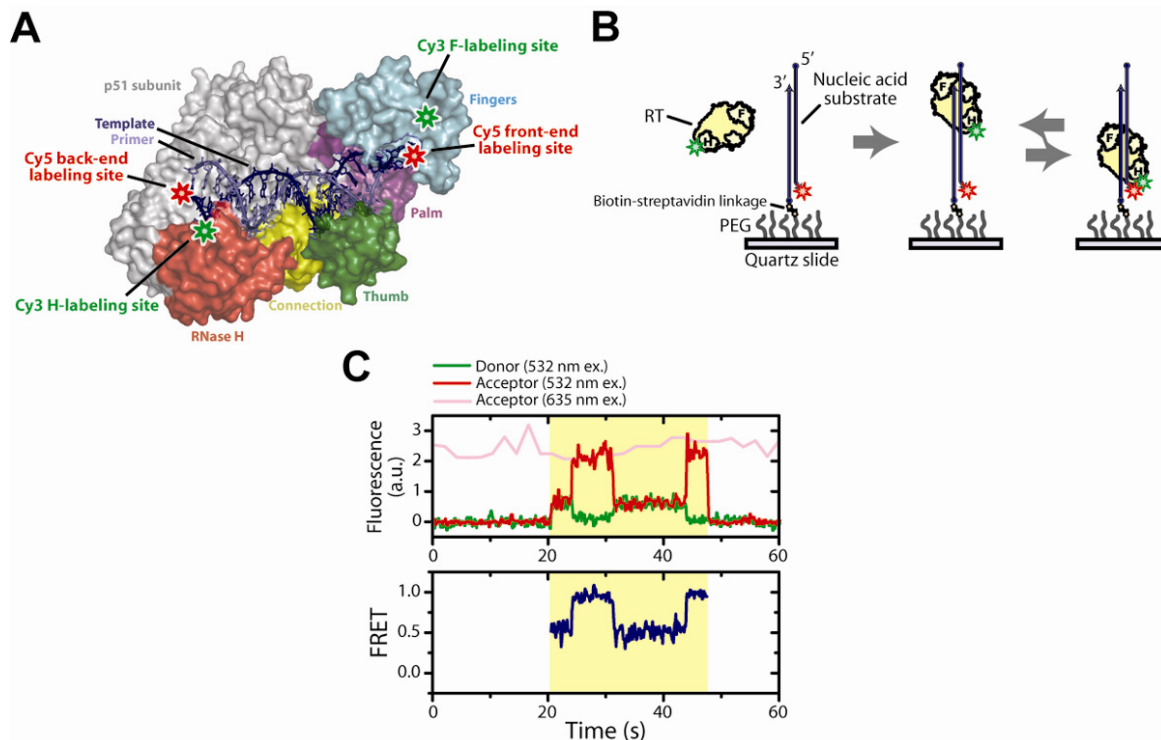


Fig. S2. Probing RT-substrate interaction in real time by single-molecule FRET. **(A)** The structure of HIV-1 RT bound to a primer/template duplex (6). The fingers, palm, thumb, connection, and RNase H domains of the p66 subunit are color-coded and the p51 subunit is in grey. The H- and F-labeling sites of the Cy3 on the enzyme are highlighted with green stars, while the front- and back-end labeling sites of Cy5 on the nucleic substrate are highlighted with red stars. **(B)** Single-molecule FRET assays for probing the enzyme-substrate interaction. The nucleic acid substrates were attached to a microscope slide surface, and binding/dissociation and motion of RT on the substrate were detected by FRET between Cy3 and Cy5. F and H on the enzyme mark the fingers and RNase H domains, respectively. **(C)** FRET analysis of individual RT binding events. (upper panel) Fluorescence time traces of a single enzyme-substrate complex. Cy5 fluorescence under 635 nm direct excitation (pink) indicates that an active Cy5-labeled substrate is present. Binding of Cy3-labeled RT leads to an increase in the total fluorescence in the Cy3 (green) and Cy5 (red) channels under 532 nm excitation. The binding event is highlighted in yellow. The FRET values during the binding event are shown in the lower panel.

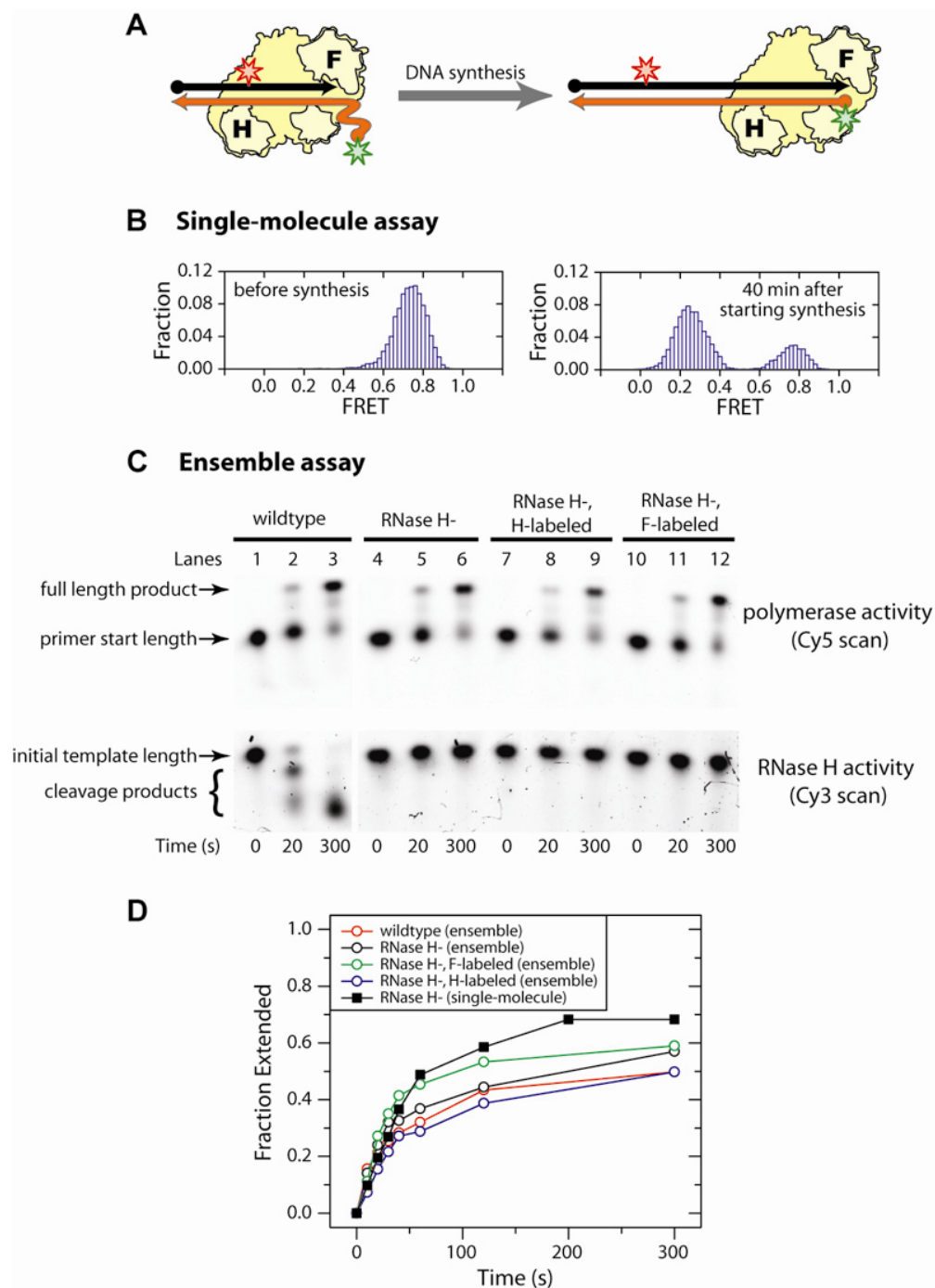


Fig. S3. Surface immobilization and dye labeling did not significantly perturb the DNA polymerase activity of RT. **(A)** To monitor the polymerase activity of the RT with single-molecule FRET, an RNA template (orange) labeled with Cy3 (green star) was annealed to a DNA primer (black) labeled with Cy5 (red star). Addition of RT (yellow) and dNTPs led to primer extension and the conversion of the single-stranded RNA region to DNA/RNA duplex,

which should increase the distance between the Cy3 and Cy5 dyes with a corresponding decrease in FRET. **(B)** FRET histograms of the surface immobilized substrates before (left) and 40 min after (right) the addition of RNase H-inactive (RNase H-) RT (20 nM) and dNTPs (200 μ M each). As expected, the FRET peak decreased from 0.76 to 0.24 upon primer extension. Primer extension kinetics were measured by recording the fraction of molecules converted from 0.76 FRET to 0.24 FRET as a function of time, as shown in black filled squares in **(D)**. **(C)** Ensemble gel electrophoresis assay for DNA polymerase and RNase H activities of four different RT constructs: unlabeled wildtype RT, unlabeled RNase H- RT, H-labeled RNase H- RT and F-labeled RNase H- RT. To initiate synthesis, RT (20 nM) and dNTPs (200 μ M each) added to the Cy3 and Cy5 doubly labeled substrates as shown in **(A)** and the reaction products were analyzed by gel electrophoresis. Primer extension was monitored by fluorescence of the Cy5-labeled primer (top panels) and the RNase H cleavage reaction was monitored by fluorescence of the Cy3-labeled RNA template (bottom panels). All four RT constructs showed substantial DNA polymerase activities, but only wildtype RT showed RNase H activity. Primer extension kinetics were measured by recording the fraction of fully-extended primer as a function of time and displayed in **(D)**. **(D)** Primer-extension kinetics measured by single-molecule FRET and ensemble gel electrophoresis. The final extent of DNA synthesis in the gel assay is slightly lower than that obtained in the single-molecule assay, likely because the unannealed primers present in the starting material would show up in the gel, but not in single-molecule assay due to the lack of FRET donor. Fitting these curves with single exponential gave extension rate constants of 0.018 sec^{-1} for unlabeled wildtype RT (ensemble), 0.018 sec^{-1} for unlabeled RNase H- RT (ensemble), 0.019 sec^{-1} for unlabeled RNase H- RT (single-molecule), 0.015 sec^{-1} for H-labeled RNase H- RT (ensemble), and 0.026 sec^{-1} for F-labeled RNase H- RT (ensemble). The primer extension kinetics are similar in all these cases, indicating that surface immobilization and dye labeling did not perturb DNA polymerase activity substantially.

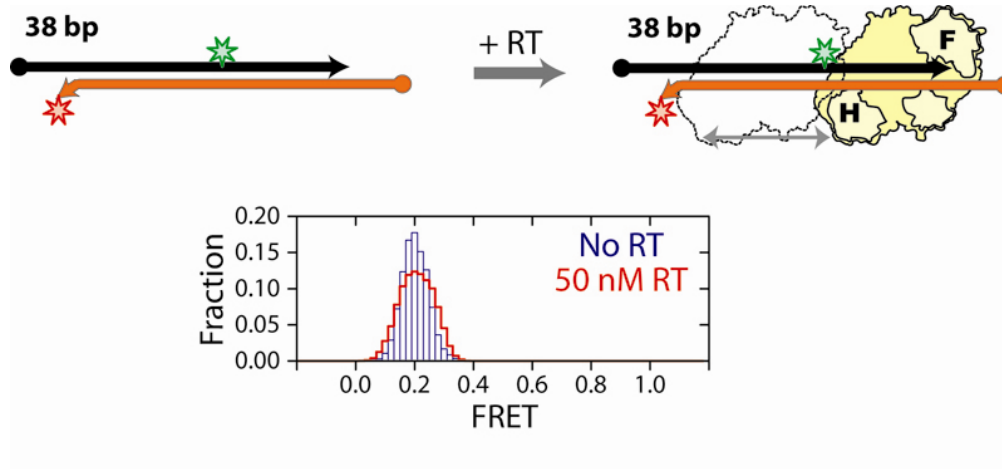


Fig. S4. Photophysical properties of the FRET dyes are not significantly altered upon RT binding. Unlabeled RT was added to the 38 bp DNA/RNA hybrid doubly labeled with Cy5 at the template 3' end spatially close to the RNase H domain of RT when the enzyme binds to the back end of the duplex, and Cy3 toward the middle of the primer spatially close to the RNase H domain of RT when it binds to the front end of the duplex. The FRET distributions were similar before (blue bars) and after (red line) the addition of 50 nM unlabeled RT, a concentration at which substrates would be in complex with RT most of the time according to a native gel shift assay. This result suggests that the photophysical properties of the dyes were not changed appreciably by RT binding.

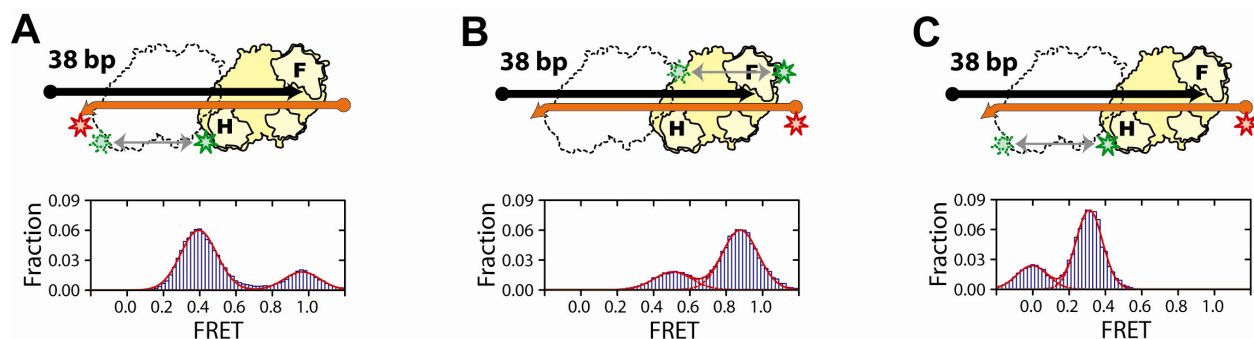


Fig. S5. Different FRET labeling scheme reveal the front-end and back-end binding states of RT on a DNA/RNA hybrid. **(A)** H-labeled RT was added to the 38 bp back-end labeled DNA/ RNA hybrid as shown in Fig. 1B. The FRET histogram (blue bars) were fit with two Gaussian peaks (red line). **(B)** F-labeled Cy3-RT was added to the 38 bp DNA/RNA hybrid with Cy5 attached to the front end of the duplex. The two binding positions at opposite ends of the hybrid would predict two FRET peaks: one peak at a high FRET value corresponding to RT bound to the front end of the hybrid with the Cy3 dye on the fingers domain close to the Cy5 dye at the substrate front end, and the other peak at a medium FRET value corresponding to RT bound to the back end of the hybrid with the Cy3 dye near the middle of the duplex. This prediction was indeed confirmed experimentally, as the measured FRET histogram (blue bars) showed high and medium FRET peaks centered at 0.88 and 0.52, respectively. **(C)** H-labeled RT was added to the front-end labeled 38 bp DNA/RNA hybrid. Again, enzyme binding at opposite ends of the hybrid would predict two FRET peaks: one at a medium FRET value corresponding to RT bound to the front end of the hybrid with the Cy3 dye on the RNase H domain near the middle of the duplex, and the other near zero FRET corresponding to RT bound to the back end of the hybrid with the Cy3 and Cy5 dyes separated by roughly the entire 38 bp length of the duplex. This prediction was also confirmed experimentally: The FRET histogram (blue bars) was fit with two Gaussian peaks centered at 0.31 and 0 (red line). In all three labeling schemes, the equilibrium constants between the front- and back-end binding states were measured to be $\sim 3:1$. While these data were obtained using the RNase H inactive RT mutant, wildtype RT yielded similar results. In the latter case, measurements were taken shortly after addition of the enzyme, before significant cleavage of the DNA/RNA hybrid could occur.

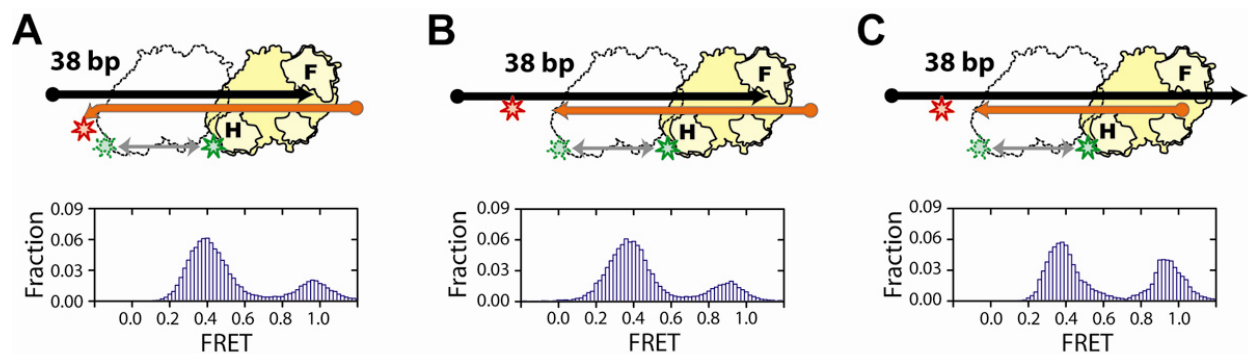


Fig. S6. Sliding dynamics of RT on DNA/RNA hybrids with different end structures. H-labeled RT was added to the back-end labeled 38 bp DNA/RNA hybrid with several distinct end structures. **(A)** A 5' overhang and 3' recess of the RNA template. A 3-nt unpaired flap is also present at the 3' terminus of the RNA template. **(B)** A 5' overhang and 3' recess of the template without a flap. **(C)** A template in which both 5' and 3' termini are recessed. In all cases, FRET was observed to transit between 0.39 and 0.95, corresponding to RT bound to the front and back ends of the hybrid region, respectively. The ratios between the areas under the 0.39 and 0.95 peaks are 3.3:1, 3.5:1, and 1.4:1, respectively. These results suggested that RT could slide on DNA/RNA hybrids with different end structures, and the relative stability of the two end binding states differed moderately depending on the end structures. The relatively higher stability of the front-end binding state in **(A)** and **(B)** suggest that the enzyme favors a recessed 3' terminus of the primer.

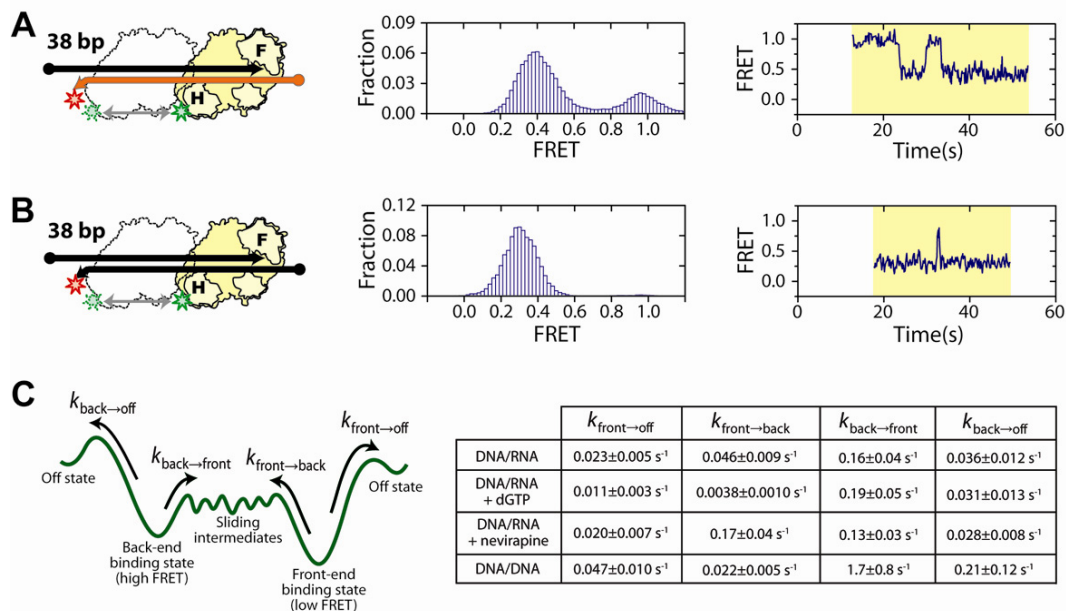


Fig. S7. Effects of duplex structures and small molecule ligands on sliding kinetics. **(A)** Sliding of RT on a 38 bp DNA/RNA hybrid. **(Left)** H-labeled RT bound to back-end labeled DNA/RNA hybrid. **(Middle)** FRET histogram. **(Right)** A representative FRET time trace showing transitions between the 0.39 and 0.95 states. **(B)** Sliding of RT on a 38 bp DNA duplex of the same sequence with the same labeling strategy. Note that the low FRET peak obtained with duplex DNA (FRET = 0.29) was lower than that of the DNA/RNA hybrid (FRET = 0.39), due to the larger inter-base distance in a duplex DNA (7, 8). The representative FRET time trace showing transitions between the 0.29 and 0.95 states on duplex DNA. **(C)** Sliding kinetics of RT on the DNA/RNA hybrid, on the DNA/RNA hybrid in the presence of 1 mM dGTP or 100 μ M nevirapine, or on the DNA duplex. **(Left)** A simple kinetic model of sliding and dissociation featuring four first-order rate constants. $k_{\text{back} \rightarrow \text{off}}$: dissociation rate constant from the back end of the duplex. $k_{\text{back} \rightarrow \text{front}}$: transition rate constant from the back to the front end. $k_{\text{front} \rightarrow \text{back}}$: transition rate constant from the front to the back end. $k_{\text{front} \rightarrow \text{off}}$: dissociation rate constant from the front end. **(Right)** Kinetic rate constants derived from the FRET time traces. Nucleotide binding reduced $k_{\text{front} \rightarrow \text{back}}$ substantially without significantly affecting $k_{\text{back} \rightarrow \text{front}}$, while nevirapine substantially increased $k_{\text{front} \rightarrow \text{back}}$ without affecting $k_{\text{back} \rightarrow \text{front}}$. Compared to the DNA/RNA hybrid case, the rate constants for escaping the back end ($k_{\text{back} \rightarrow \text{front}}$ and $k_{\text{back} \rightarrow \text{off}}$) were much higher for duplex DNA. Detailed analysis methods were described in Materials and Methods.

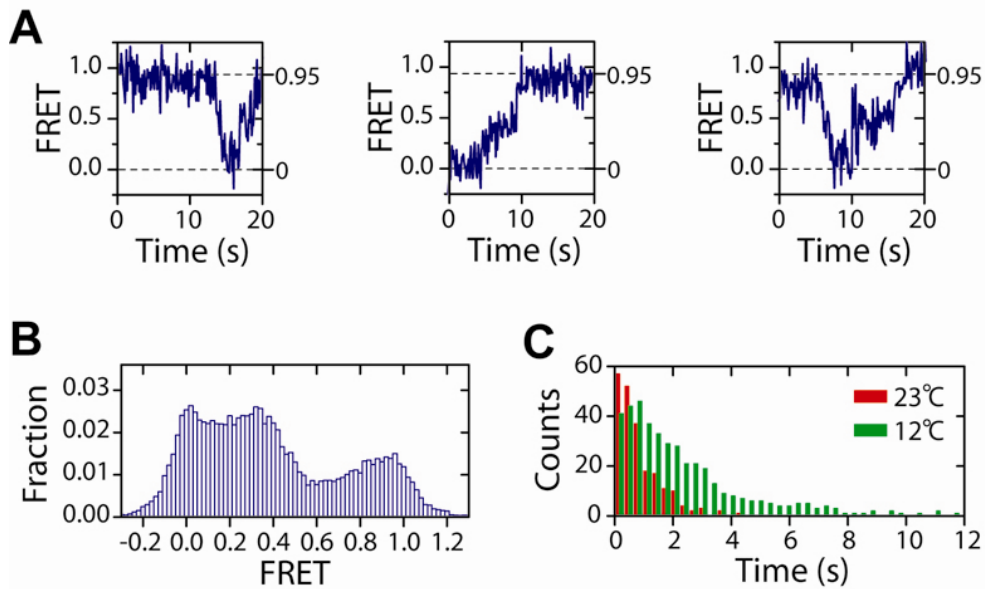


Fig. S8. RT shuttles between the two ends of the DNA/RNA hybrid with preferred intermediate states. **(A)** Additional FRET time traces showing RT sliding on a 56 bp DNA/RNA hybrid at 12 °C. Another trace is shown in Fig. 1D. These traces reveal gradual transitions between the 0 FRET (front-end binding) and 0.95 FRET (back-end binding) states and preferred intermediates near FRET $\sim 0.3 - 0.5$. **(B)** FRET histogram constructed from multiple transition regions. The histogram also includes 25 frames before and after each transition region to show the two end-bound states (FRET = 0 or 0.95). A predominant intermediate peak at FRET $\sim 0.3 - 0.5$ was observed. **(C)** Histograms for the transition time between the 0 and 0.95 FRET states at 23 °C (red bars) and 12 °C (green bars). The mean transition time was 0.88 sec at 23 °C, and 2.6 sec at 12 °C.

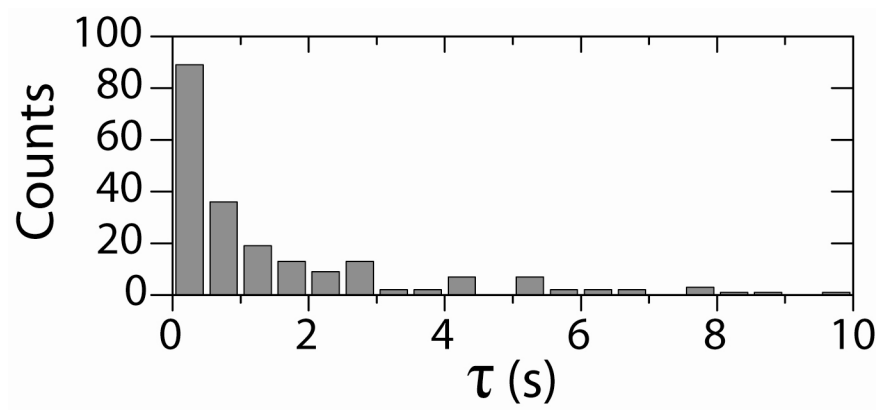


Fig. S9: The histogram of the time delay τ between binding of RT and placing of RT at the polymerization site as observed in Figure 2.

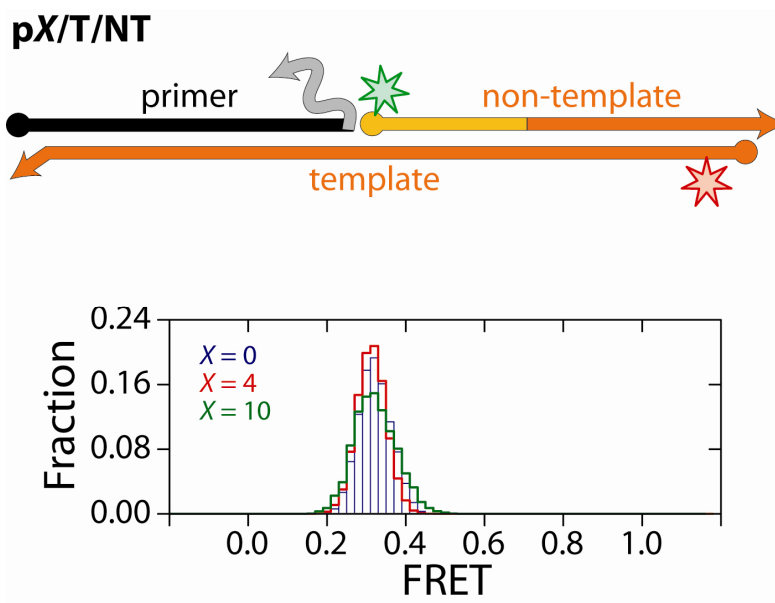


Fig. S10. The FRET distributions of the RNA strand displacement substrates $pX/T/NT$, each consisting of an RNA template (T) to which a complementary DNA primer (p) and RNA non-template strand (NT) were simultaneously hybridized, with the Cy3 and Cy5 dyes flanking the T/NT duplex region. Overlapping regions between the DNA primer and the RNA non-template strand are colored in light grey and orange, respectively. We use the notation $pX/T/NT$ to represent a substrate whose primer has been extended by X nucleotides. Here $X = 0, 4$, and 10 . The FRET measurements were obtained in the absence of RT.

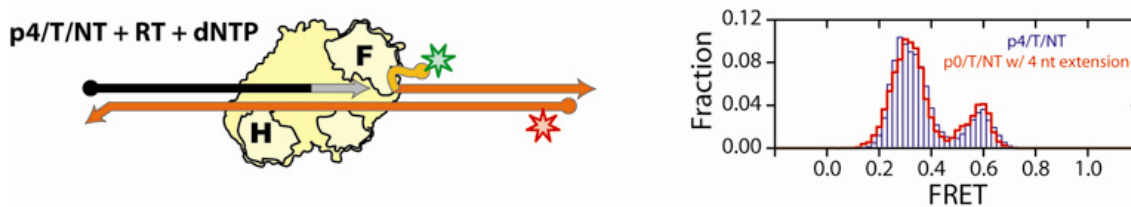


Fig. S11. Structural dynamics of RNA displacement substrates in the presence of RT. RT and dNTPs were added to the p4/T/NT substrate doubly labeled with Cy3 and Cy5. The primer strand was chain-terminated to prevent extension. DNA and RNA strands are colored in black and orange, respectively. Overlapping regions between the DNA primer and the RNA non-template strand are colored in light grey and orange, respectively. The FRET histogram (blue bars) shows two peaks at 0.3 and 0.6 and FRET time traces (not shown) reveal transitions between the two states. The histogram agrees quantitatively with the one obtained for the p0/T/NT substrate once dCTP, dGTP, dATP, and ddTTP were added to allow 4-nucleotide extension of the p0 primer (red line). The latter histogram is also shown in Fig. 3B.

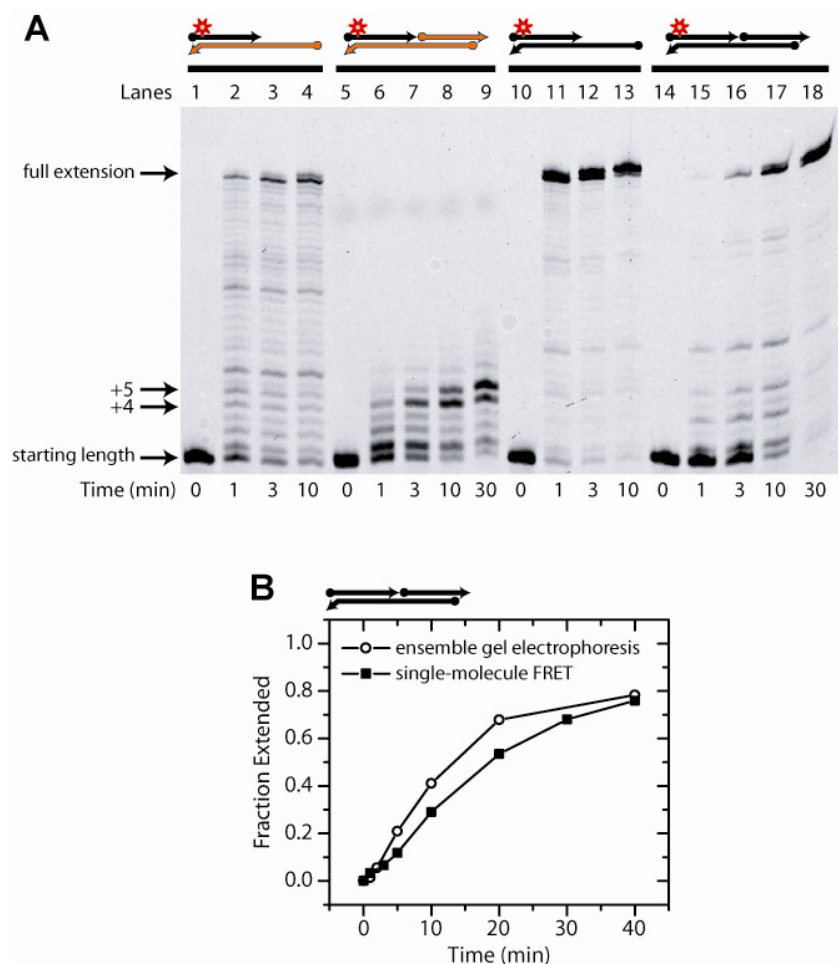


Fig. S12. Comparison of normal and strand displacement synthesis. **(A)** Primer extension assays for RNA-directed DNA synthesis (lanes 1-4), RNA strand displacement synthesis (lanes 5-9), DNA-directed DNA synthesis (lanes 10-13), and DNA strand displacement synthesis (lanes 14-18). The extended primer was monitored by Cy5 fluorescence. As shown in the gel, both RNA-directed (lanes 1-4) and DNA-directed (lanes 10-13) DNA synthesis are highly efficient with rapid accumulation of full length product. In the case of strand displacement synthesis, RT supported limited RNA strand displacement synthesis, terminating predominantly after extension of the primer by 5 nt (lanes 5-9). The exact termination site was sequence dependent (data not shown). In contrast, the primer was fully extended during DNA strand displacement synthesis (lanes 14-18). **(B)** Primer extension kinetics of DNA displacement synthesis measured by ensemble gel electrophoresis (as shown in **A**) and single-molecule FRET (Fig. 5C). The fraction of primers fully extended by RT was plotted as a function of time. Similar primer extension kinetics were observed with the two methods.

REFERENCES

1. J. W. Rausch, B. K. Sathyanarayana, M. K. Bona, S. F. Le Grice, *J Biol Chem* **275**, 16015 (2000).
2. J. Winshell, B. A. Paulson, B. D. Buelow, J. J. Champoux, *J Biol Chem* **279**, 52924 (2004).
3. E. A. Abbondanzieri *et al.*, *Nature* **453**, 184 (2008).
4. I. Rasnik, S. A. McKinney, T. Ha, *Nat Methods* **3**, 891 (2006).
5. A. Telesnitsky, S. P. Goff, in *Retroviruses* J. M. Coffin, S. H. Hughes, H. E. Varmus, Eds. (Cold Spring Harbor Laboratory Press, 1997) pp. 121-160.
6. S. G. Sarafianos *et al.*, *Embo J* **21**, 6614 (2002).
7. O. Fedoroff, M. Salazar, B. R. Reid, *J Mol Biol* **233**, 509 (1993).
8. N. C. Horton, B. C. Finzel, *J Mol Biol* **264**, 521 (1996).